DOI: 10.26599/FSHW.2026.9250943

Contents lists available at SciOpen

Food Science and Human Wellness

journal homepage: https://www.sciopen.com/journal/2097-0765

China Food Publishing Co.

Honey as a natural absorption enhancer: Mechanisms underlying the improved oral bioavailability and bioactivity of *Astragalus* flavonoids

Weiye Zhang[#], Xiao Su[#], Guangmin Liu, Yanjun Yang, Zhubin Zhang, Xiaobin Jia[*], Liang Feng[*], Bing Yang[*]

School of Traditional Chinese Pharmacy, State Key Laboratory of Natural Medicines, China Pharmaceutical University, Nanjing 211198, P.R. China

ABSTRACT: *Astragalus* is a functional plant with notable medicinal and nutraceutical value, and its combination with honey represents a classic pairing in traditional dietary therapy. To address the low oral bioavailability of *Astragalus* flavonoids (AFs, including calycosin-7-*O*-*β*-*D*-glucoside, ononin, calycosin, and formononetin), the primary bioactive components of *Astragalus*, our study demonstrated that honey significantly increases the systemic exposure of AFs, thereby enhancing oral bioavailability. These enhancement effects are attributed to the supramolecular structures in honey that interact with AFs through intermolecular non-covalent interactions, and reversible modulation of tight junction barriers by honey, which facilitates the paracellular absorption of AFs. Furthermore, honey's absorption-enhancing effects were validated by the enhanced Qi-tonifying (enhancement of the body's vital energy to defend illnesses) efficacy observed in the AFs-honey combination. Our findings provide scientific references for the potential application of honey as a natural absorption enhancer, while offering novel insights into the traditional combination of *Astragalus* and honey.

Keywords: *Astragalus* flavonoids; honey; oral bioavailability; intermolecular non-covalent interactions; tight junction barriers; bioactivity

1. Introduction

Astragalus, as a traditional medicinal and edible homologous plant, holds important application value in both traditional Chinese medicine (TCM) and modern functional food industries[1,2]. Current research has demonstrated that *Astragalus* exhibits multiple bioactivities, including anti-inflammatory, anti-oxidant, anti-tumor, immunomodulatory, and cardioprotective effects[3-6]. As a raw material for functional foods, *Astragalus* has been widely used in herbal teas, therapeutic foods, and nutritional supplements[7,8], demonstrating favorable effects as a daily intervention for sub-healthy populations, frail elderly individuals, and immunocompromised patients with chronic diseases. The primary bioactive components of *Astragalus* include flavonoids, triterpenoid saponins, polysaccharides, amino acids, and various trace elements[9,10]. Notably, accumulating evidence confirms that *Astragalus* flavonoids (AFs), as crucial secondary metabolites,

***Corresponding author**
Bing Yang, 15751151582@163.com.
Liang Feng, wenmoxiushi@163.com.
Xiaobin Jia, jiaxiaobin2015@163.com.

Received 14 August 2025
Received in revised from 24 September 2025
Accepted 7 October 2025

represent the fundamental active substances responsible for the bioactivities of *Astragalus*. To date, over 30 kinds of flavonoids have been identified in *Astragalus*, with calycosin-7-*O*-*β*-*D*-glucoside (CAG), ononin (ON), calycosin (CA), and formononetin (FMN) being the principal isoflavonoids that have been validated as key small-molecule bioactive constituents[11-14]. However, due to their complex chemical structures, these flavonoids generally exhibit low prototype absorption rates and poor bioavailability, which presents a significant challenge for their application[14].

Honey is a natural food produced by bees through the collection of floral nectar or plant secretions (e.g., honeydew), followed by enzymatic digestion, concentration, and storage. It is highly valued for its distinctive flavor profile, rich nutritional composition, and potential health benefits[15-17]. In China, the combination of honey and *Astragalus* represents a classic pairing in traditional dietary therapy, and honey-processed *Astragalus* demonstrates superior efficacy in Qi-tonifying (enhancement of the body's vital energy to defend illnesses) and immunomodulation. Contemporary research has revealed honey's potential as a bioavailability enhancer for small-molecule constituents. For instance, honey possesses natural deep eutectic solvent (NADES) characteristics, which significantly improve the solubility and extraction efficiency of polyphenols, flavonoids, and saponins[18-20]. Moreover, honey contains abundant monosaccharides, disaccharides, and phenolic compounds that form extensive hydrogen-bond networks, providing the structural basis for interactions with small-molecule bioactive constituents[21]. Notably, honey has been shown to markedly improve the bioavailability of acyclovir, which is attributed to its modulation of intestinal epithelial tight junction integrity[22]. These findings raise important scientific questions: Does honey significantly enhance the oral bioavailability of AFs, and if observed, is this potential enhancement mediated by molecular interactions and intestinal regulation?

This study aims to systematically elucidate the absorption-enhancing effects of honey on AFs and the underlying mechanisms. Initially, the effects of honey on the oral bioavailability of AFs were evaluated. Subsequently, the molecular interactions between honey and AFs were investigated from multiple perspectives, with emphasis on their effects on the solubility, permeability, and stability of AFs. Furthermore, a Caco-2 cell transport model was employed to delineate the mechanisms underlying honey-enhanced AFs absorption, which involved both transmembrane transport and paracellular pathways. Finally, honey's absorption-enhancing effects were validated through assessing the effects of honey on the Qi-tonifying efficacy of AFs. This study not only provides a theoretical foundation for developing honey as a natural absorption enhancer but also offers novel insights into the traditional combination of *Astragalus* and honey.

2. Materials and Methods

2.1 Materials

Chinese vitex honey (monofloral honey from *Vitex negundo* var. *heterophylla*, Lamiaceae) was provided by the Institute of Apicultural Research, Chinese Academy of Agricultural Sciences (IAR-CAAS). CAG, ON, CA, FMN, and baohuoside II (purity ≥ 98% for all) were obtained from Chengdu Pufei De Biotech Co., Ltd. (Chengdu, China). Baohuoside I (purity ≥ 98%) was obtained from Nanjing Kasaisi Pharmaceutical

Technology Co., Ltd. (Nanjing, China). AFs (containing CAG, ON, CA, and FMN at purity ≥ 63.8%) were isolated and purified, and the remaining aliquots were stored in our laboratory. Fluorescein sodium, fluorescein potassium, Matrigel®, and verapamil were purchased from MedChemExpress (MCE, USA). Probenecid and dipyridamole were purchased from Shanghai Yuanye Biotechnology Co., Ltd. (Shanghai, China). Primary antibodies including rabbit anti-ZO-1, anti-occludin, anti-claudin-1, and anti-β-catenin were sourced from Proteintech Group, Inc. (Wuhan, China). Secondary reagents including Cy3-conjugated goat anti-rabbit IgG (H+L), DAPI staining solution, antifade mounting medium, and Triton X-100 permeabilization buffer were obtained from Beyotime Biotechnology (Shanghai, China). Other chemical reagents were analytical grade.

2.2 Animals and cell culture

The A549-Luc cell line was purchased from QuiCell Biotechnology Co., Ltd. (Shanghai, China). Caco-2 cells were obtained from Vigen Biotechnology Co., Ltd. (Zhenjiang, China). Fetal bovine serum (FBS) was acquired from OZfan Biological Technology Co., Ltd. (Nanjing, China).

Male BALB/c nude mice (4 weeks, 18–22 g) and male Sprague-Dawley (SD) rats (250 ± 20 g) were purchased from Huachuang Sino Pharmaceutical Technology Co., Ltd. (Jiangsu, China). The animals were maintained under standardized conditions with a 12/12-hour light/dark cycle, temperature of 24 ± 2 ℃, relative humidity of 55 ± 5%, and *ad libitum* access to autoclaved food and purified water.

All animal experiments were approved by the Institutional Animal Care and Use Committee (IACUC) of China Pharmaceutical University (Approval No. 2024-06-21) and conducted in strict compliance with Chinese national regulations, specifically the “Guidelines for Ethical Review of Laboratory Animal Welfare” (GB/T 35892-2018) and the “Guidelines for Humane Endpoints in Animal Experiments” (RB/T 173-2018). All procedures adhere to the European Community guidelines (Directive 2010/63/EU) for the protection of animals used in scientific research. Throughout the study, maximal efforts were undertaken to uphold the highest standard of animal welfare and ethical treatment.

2.3 Effects of Honey on the Oral Bioavailability of AFs

Male SD rats were fasted for 16 h and then randomly divided into two groups (n = 6): the AFs group and the AFs-honey group. The AFs group received an oral gavage of 100 mg/kg AFs, while the AFs-honey group received 100 mg/kg AFs combined with 100 mg/kg honey via oral gavage. Under anesthesia, blood samples were collected via the orbital venous plexus at predetermined time intervals (0, 5, 15, 30, 45, 60, 120, 240, 360, and 480 min) into heparin-coated centrifuge tubes. The collected blood samples were allowed to stand for 30 min and then centrifuged at 3000 rpm for 10 min at 4 ℃ to separate the plasma, which was subsequently stored at -80 ℃ until LC-MS/MS analysis.

2.4 Molecular interactions study

2.4.1 Preparation of AFs-honey aggregates

Honey was dissolved in deionized water to prepare solutions at concentrations of 10 mg/mL, 20 mg/mL, 30 mg/mL, and 40 mg/mL. AFs (50 mg) were then dissolved in either water or honey solutions (5 mL), resulting in AFs-to-honey mass ratios of 1:0, 1:1, 1:2, 1:3, and 1:4, respectively. The mixtures were shaken in a constant temperature water bath at 37 ℃ for 24 h and then centrifuged at 4000 rpm for 10 min. The supernatant was collected to obtain the AFs-honey aggregates. Some of the samples were lyophilized for subsequent analysis.

2.4.2 Critical aggregation concentration (CAC) determination

The CAC was determined using pyrene as a fluorescence probe. Pyrene solution (50 μL, 12×10^{-3} mg/mL in acetone) was added to a series of 1 mL brown volumetric flasks, and the acetone was evaporated under nitrogen gas. Varying volumes of honey solutions (128 mg/mL) were added and diluted with deionized water to achieve final honey concentrations of 0.01, 0.1, 0.5, 1, 2, 8, 16, 32, and 64 mg/mL. The solutions were shaken in the dark for 30 min and then incubated in a water bath at 60 ℃ for 3 h, followed by cooling to 40 ℃. Fluorescence spectra were recorded using a fluorescence spectrophotometer (RF-5301, Shimadzu, Japan) with an excitation wavelength of 333 nm and an emission range of 340–450 nm. The CAC of honey was determined by analyzing the fluorescence intensity ratio of the first peak (I_1, 373 nm) to the third peak (I_3, 384 nm) in relation to the logarithmic values of honey concentration (log$C$). The CAC of the AFs-honey aggregates was determined using the same method, with final aggregates concentrations of 10^{-4}, 10^{-3}, 10^{-2}, 10^{-1}, 0.25, 0.5, 1, 2 mg/mL.

2.4.3 Morphology, structure, and physical properties characterization

The microstructure of the samples was observed by TEM (HT7700, Hitachi, Ltd., Japan) after 2% phosphotungstic acid staining at an acceleration voltage of 120 kV. The surface morphology was characterized by SEM (Regulus-8100, Hitachi, Ltd., Japan) after gold sputtering for 1 min. The z-average size, particle size distribution, polydispersity index (PDI), and ζ potential of the samples were measured using a Zetasizer Nano ZS instrument (ZEN3600, Malvern, UK).

2.4.4 Spectroscopic analysis

The XRD patterns of the samples were recorded using an X-ray diffractometer (SmartLab SE, Rigaku, Ltd., Japan) equipped with a Cu-Kα monochromator. The operating conditions were as follows: tube voltage of 40 kV, tube current of 50 mA, and a diffraction angle range of 3° to 50°. The functional groups and chemical bonds of the samples were analyzed by FT-IR spectroscopy (Tensor 27, Bruker, Germany). Honey was analyzed using the ATR mode due to its high viscosity, while the other sample powders were mixed with potassium bromide for analysis. The scanning conditions were as follows: wavenumber range of 4000 to 400 cm^{-1}, resolution of 4 cm^{-1}, scanning speed of 10 kHz, and a total of 32 scans.

2.4.5 Thermal analysis

The thermal stability and behavior of the samples were analyzed by TGA (TGA 4000, PerkinElmer, USA) and DSC (DSC 3500 Sirius, Netzsch, Germany). The experimental conditions were as follows: dynamic nitrogen atmosphere (99.999%), temperature range of 30 to 500 ℃, and a heating rate of 20 ℃/min.

2.4.6 Molecular dynamics (MD) simulation

Three-dimensional molecular structures of honey components were constructed using Materials Studio 2020 (Accelrys, USA) and geometrically optimized with ultra-fine precision using the Smart method. The Forcite module and the COMPASS III force field were employed to perform microcanonical ensemble (NVE) MD simulations at 298 K for a total duration of 500 ps, with a time step of 1 fs. Electrostatic interactions were calculated using the Ewald summation method, while van der Waals forces were computed using an atom-based method with a cutoff radius of 18.5 Å. Hydrogen bond interactions were separately evaluated using the Dreiding force field. Additionally, the DMol3 module was used to calculate the electrostatic potentials of glucose, fructose, and their combined system based on density functional theory (DFT) with the GGA functional and the PW91 basis set. All molecular optimizations were performed at the GGA/PW91 level. Finally, the adsorption characteristics of AFs on the stable honey system were simulated, and their interaction energies with the honey structure were analyzed.

2.5 Determination of equilibrium solubility

The effects of honey on the equilibrium solubility of AFs in water were investigated using the saturated shake flask method. Excess AFs (12 mg) were added to closed conical flasks containing 1 mL of deionized water or honey solution (12 mg/mL). The flasks were then shaken in a thermostatic oscillator at 37 ℃ and 120 rpm for 24 h to achieve equilibrium and saturation. The supernatant was collected, treated with methanol, filtered through a 0.22 μm microporous membrane, and analyzed using HPLC.

2.6 Study on stability in simulated gastrointestinal fluids

Artificial gastric juice, small intestinal fluid, and colonic fluid were prepared according to the Chinese Pharmacopoeia (2020). AFs were added alone or in combination with honey to these fluids and agitated in a thermostatic oscillator at 37 ℃ and 120 rpm to simulate the degradation of bioactive constituents in the gastrointestinal tract. With reference to the typical residence times of constituents in various gastrointestinal segments (stomach: 1–4 h; small intestine: 2–6 h; colon: 12–48 h), samples were collected after 4 h of incubation in the gastric environment, 6 h in the small intestinal environment, and 24 h in the colonic environment.

2.7 Parallel artificial membrane permeability assay (PAMPA)

The PAMPA method was consistent with our previous study. The permeable diffusion cell comprised two cylindrical glass chambers separated by a central PVDF membrane, creating a donor chamber and a receptor chamber. A clear 4% egg yolk lecithin-dodecane solution (artificial membrane solution, 500 μL) was applied to the PVDF membrane to simulate a biological membrane. The donor chamber received solutions of AFs or AFs-honey, while the receptor chamber contained a blank solvent. The apparatus was incubated at

37 ℃ and 300 rpm for 12 h, after which samples were collected at different time points for HPLC analysis. The effective permeability of the AFs was calculated using the following equations:

(1)

$$C_e = \frac{C_d \cdot V_d + C_a \cdot V_a}{V_d + V_a}$$

(2)

$$\text{Effective permeability (\%)} = \frac{C_a}{C_e} \times 100\%$$

C_e: the theoretical equilibrium concentration at time t; C_a: AFs concentration in the receptor chamber at time t; C_d: AFs concentration in the donor chamber at time t; V_a: liquid volume in the receptor chamber; V_d: liquid volume in the donor chamber.

2.8 Single-pass intestinal perfusion (SPIP) model study

Male SD rats were fasted for 16 h and then randomly divided into two groups (n = 4): the AFs group and the AFs-honey group. Rats were anesthetized by intraperitoneal injection of 2% sodium pentobarbital (0.3 mL/100 g). Flexible PVC tubes were used to cannulate the duodenum, jejunum, ileum, and colon (approximately 10 cm per segment) with the inlet connected to a peristaltic pump (BT100-1F, Halma, UK). Each intestinal segment was flushed with sterile saline, and the incision sites were covered with saline-soaked gauze. The intestine was saturated with Krebs-Ringer (K-R) solution for 10–15 min, followed by perfusion with K-R solution containing AFs (2 mg/mL) or AFs-honey (AFs: 2 mg/mL, honey: 2 mg/mL) at a flow rate of 0.2 mL/min. After reaching steady state, samples were collected every 30 min for 2 h. At the end of the experiment, the masses of the perfusate at the inlet and outlet were measured. Following deep anesthesia, euthanasia was performed via cervical dislocation, with subsequent documentation of each perfused intestinal segment's length (l) and cross-sectional radius (r). The effective permeability coefficient (P_{eff}) and absorption rate constant (K_a) of the AFs were calculated using the following equations:

(3)

$$P_{eff} = \frac{-Q_{in} \ln\left(\frac{C_{out}}{C_{in}} \times \frac{V_{out}}{V_{in}}\right)}{2\pi r l}$$

(4)

$$K_a = \frac{\left(1 - \frac{C_{out}}{C_{in}} \times \frac{V_{out}}{V_{in}}\right)}{\pi r^2 l} Q_{in}$$

V_{in} and V_{out}: the volumes of the perfusate at the inlet and outlet; C_{in} and C_{out}: the concentrations of AFs in the perfusate at the inlet and outlet; Q_{in}: the flow rate of the perfusion.

2.9 Establishment and characterization of Caco-2 cell monolayer model

Caco-2 cell suspensions (5×10^5 cells/mL) were seeded onto Transwell chambers with PET membranes at a density of 0.5 mL/well and cultured for 21 days in a humidified atmosphere of 5% CO_2 at 37 ℃ to establish a monolayer model. During the cultivation period, transepithelial electrical resistance (TEER) values

were monitored every 2–4 d using an epithelial voltohmmeter (Millicell® ERS-2, Millipore, USA). The alkaline phosphatase (ALP) activity of the cell monolayer was determined using an assay kit (Cat.No.P0321S, Beyotime, China), and sodium fluorescein permeability assays were conducted to validate the monolayer integrity. On day 21, the ultrastructure was examined by SEM (Regulus-8100, Hitachi, Ltd., Japan) and TEM (HT7700, Hitachi, Ltd., Japan).

2.10 Bidirectional transport experiments

Well-differentiated Caco-2 cell monolayers with TEER values exceeding 600 Ω·cm² were selected for the bidirectional transport studies. The monolayers were gently washed three times with pre-warmed PBS (pH = 7.4) and then equilibrated in a humidified incubator (37 ℃, 5% CO_2) for 30 min. Donor solutions were added to either the apical (AP) or basolateral (BL) side, while the opposite compartment received an isotonic, serum-free medium with maintained volumes of 0.5 mL (AP) to 1.5 mL (BL). After 6 h of incubation, 200 μL samples were carefully collected from the receiving chamber for HPLC analysis. To investigate the effects of honey on the intestinal transport of AFs, the following experimental groups were established: a baseline transport group containing an 800 μg/mL AFs (with or without 20 mg/mL honey), and efflux protein inhibition groups comprising an 800 μg/mL AFs supplemented with either 100 μmol/L verapamil (P-gp inhibitor), 100 μmol/L probenecid (MRP inhibitor), or 10 μmol/L dipyridamole (BCRP inhibitor), each with parallel controls with or without 20 mg/mL honey. The apparent permeability coefficient (P_{app}) and efflux ratio (ER) were calculated using the following equations:

(5)

$$P_{app}=\frac{\Delta Q}{(\Delta t\times A\times C_0)}$$

(6)

$$ER=\frac{P_{app}(BL\rightarrow AP)}{P_{app}(AP\rightarrow BL)}$$

ΔQ: the cumulative amount of AFs transported; Δt: the transport time; A: the surface area of the PET membrane (1.12 cm²); C_0: the initial AFs concentration in either the AP or BL side; P_{app}(AP→BL): the P_{app} of the AP→BL direction; P_{app}(BL→AP): the P_{app} of the BL→AP direction.

2.11 Transepithelial electrical resistance (TEER) measurement

The TEER values were measured at baseline and at 20, 40, 60, 80, 100, and 120 min after the addition of honey solution (20 mg/mL) to the AP side using an epithelial voltohmmeter (Millicell® ERS-2, Millipore, USA). Following the assay, cell monolayers were gently rinsed with pre-warmed PBS (pH = 7.4) and maintained in fresh complete medium for 24 h before final TEER measurement.

2.12 Immunofluorescence staining

After 3 washes with pre-warmed PBS (pH = 7.4), 20 mg/mL honey solution was added to the AP side. Caco-2 cell monolayers were collected at baseline and 2 h post-treatment. An additional experimental group was treated with honey solution for 2 h, then replaced with fresh complete medium until 24 h before sampling.

Collected cell monolayers were fixed with 4% paraformaldehyde for 20 min, permeabilized with 0.1% Triton X-100 for 20 min, and blocked with 2% BSA for 1 h at room temperature. Subsequently, cell monolayers were incubated at 37 ℃ with rabbit primary antibodies against β-catenin (1:200), occludin (1:500), claudin-1 (1:200), and ZO-1 (1:100). After treatment with Cy3-conjugated goat secondary antibody (1:500) for 1 h at 37 ℃ in dark, nuclei were stained with DAPI. Finally, cell monolayers were mounted on slides using antifade mounting medium and visualized under a confocal laser scanning microscope (STELLARIS 5, Leica, Germany) to examine the fluorescence expression of β-catenin, occludin, claudin-1, and ZO-1.

2.13 Animal experiments

2.13.1 Establishment of an orthotopic lung tumor-induced Qi deficiency syndrome model in nude mice

Following anesthesia with 3% isoflurane (1 L/min O_2), nude mice were positioned in left lateral recumbency on a surgical board. A 5-mm skin incision was made at the intersection of the elbow joint and scapular posterior border extension line using ophthalmic scissors. Muscle tissue was bluntly dissected with forceps until exposure of the pleura and ribs. An insulin syringe needle was inserted at a 30° angle through the intercostal space into the left lung, followed by slow injection of 50 μL cell suspension (1×10^6 A549-Luc cells). The incision was sutured and disinfected with povidone-iodine postoperatively.

2.13.2 Experimental design

One week after surgery, a total of 48 nude mice successfully injected with A549-Luc cells were randomly divided into eight groups ($n = 6$): the model group, the cisplatin (CDDP) group, the Bufei pill (BFP) group, the AFs-low dose (AFs-L) group, the AFs-honey-low dose (AFs-honey-L) group, the AFs-high dose (AFs-H) group, the AFs-honey-high dose (AFs-honey-H) group, and the honey group. CDDP was chosen as a benchmark for antitumor activity owing to its established efficacy as a widely used platinum-based chemotherapeutic agent in non-small cell lung cancer (NSCLC). In parallel, BFP served as a positive control given its documented lung-strengthening and Qi-tonifying effects in treating lung Qi deficiency (manifested as chronic cough, shortness of breath, and dyspnea), making it a relevant comparator for evaluating the Qi-tonifying efficacy of AFs. The main components of BFP include *Rehmanniae Radix Praeparata*, *Codonopsis Radix*, *Astragali Radix*, *Mori Cortex*, *Asteris Radix*, and *Schisandrae Chinensis Fructus*. An additional six healthy nude mice served as the control group. The CDDP group was intraperitoneally administered CDDP (3 mg/kg), whereas the BFP group received BFP (2.34 g/kg) by oral gavage. The AFs-L and AFs-H groups were treated with AFs at doses of 12 and 36 mg/kg, respectively, via gavage. The AFs-honey-L and AFs-honey-H groups received the same AFs doses (12 or 36 mg/kg) coadministered with honey (300 or 900 mg/kg). The honey group was administered honey alone (900 mg/kg). Both the control and model groups were given an equal volume of 0.9% saline daily through oral gavage for three weeks. After the final administration, pulmonary function tests, *in vivo* imaging, and Micro-CT scanning were performed. Following deep anesthesia with sodium pentobarbital, nude mice underwent aseptic blood collection via abdominal aorta puncture. Euthanasia was then performed by cervical dislocation, with subsequent complete excision of splenic and pulmonary tissues.

2.13.3 Determination of spleen index (SI)

The body weights of nude mice and the wet weights of the spleens were measured. The SI was calculated using the following equation:

(7)

$$SI=\frac{\text{Spleen weight (mg)}}{\text{Body weight (g)}}$$

2.13.4 Assessment of pulmonary function

Pulmonary function was assessed in nude mice from each group using a whole-body plethysmography system (EMKA-PLT-WBP, France). The conscious and freely moving mice were placed in the whole-body plethysmography chamber. After stabilization, pulmonary function parameters were continuously monitored for 5 min, and mean values were calculated.

2.13.5 Arterial blood gas (ABG) analysis

Following anesthesia, approximately 0.3 mL of arterial blood was collected from the abdominal aorta using a single-use arterial blood sampler and immediately transferred into a G3+ blood gas test cartridge. Arterial partial pressure of oxygen (PO_2) and carbon dioxide (PCO_2) were analyzed using a blood gas analyzer (i-STAT 300-G, Abbott, USA).

2.13.6 Histopathological examination of lung tissue

Following euthanasia, intact lung tissues were harvested, rinsed with sterile physiological saline, and macroscopically examined for pathological alterations. The tissues were then fixed in 10% neutral buffered formalin (NBF) and processed according to conventional paraffin-embedding protocols. Tissue sections were stained with hematoxylin and eosin (H&E) and observed under a microscope (KF-PRO-120, JiangFeng Biotechnology, China).

2.13.7 Observation of pulmonary tumor growth

In vivo imaging: Fifteen minutes before imaging, nude mice received an intraperitoneal injection of fluorescein potassium (150 mg/kg). Under isoflurane anesthesia, bioluminescent signals from pulmonary tumors were measured using an *in vivo* imaging system (IVIS, ABL-X6, Tanon Life Science Co., Ltd., China) with a 15-s exposure time in bioluminescence mode.

Micro-CT scanning: Following isoflurane anesthesia, the lungs of nude mice were scanned using Micro-CT (SKYSCAN 1276, Bruker, Germany). The scanning parameters were: tube voltage, 55 kV; tube current, 200 μA; resolution, 36 μm; aluminum filter, 0.25 mm; radiation dose, 500 mGy.

2.14 Analysis methods

2.14.1 LC-MS/MS analysis

For bioavailability studies, 10 μL of internal standard (IS) solution (Baohuoside II, 173.6 ng/mL in acetonitrile) and 500 μL of acetonitrile were added to 100 μL of plasma samples, followed by ultrasonication (40 kHz, 25 ℃, 30 min) and centrifugation (13,000 rpm, 4 ℃, 10 min). The supernatants were collected and

evaporated to dryness under nitrogen. The residues were redissolved in 150 μL of acetonitrile and recentrifuged. The final supernatants were transferred into chromatographic sample bottles for LC-MS/MS analysis.

Samples were analyzed using an Agilent 6470 triple quadrupole LC-MS/MS system equipped with an ACQUITY UPLC® BEH C_{18} column (2.1 mm × 50 mm, 1.7 μm) maintained at 40 ℃. The mobile phase consisted of 0.1% (*v*/*v*) formic acid in water (A) and acetonitrile (B), with the following gradient program: 0–1.0 min,15% B; 1.0–1.5 min, 15%–40% B; 1.5–4.5 min, 40% B; 4.5–7.0 min, 40%–100% B; 7.0–8.0 min, 100% B; 8.0–8.5 min, 100%–15% B; 8.5–10.0 min, 15% B. The flow rate was maintained at 0.3 mL/min with an injection volume of 3 μL. Mass spectrometer detector was performed using an electrospray ionization (ESI) source in positive ion mode with the following parameters: sheath gas temperature, 230 ℃; gas temperature, 300 ℃; gas flow, 15 L/min; nebulizer pressure, 45 psi; capillary voltage, 3500 V; fragmentor voltage, 80 V (Baohuoside II), 100 V (CAG and ON), 125 V (CA), 120 V (FMN); collision energy, 16 V (Baohuoside II), 30 V (CAG, ON, CA, and FMN). The precursor-to-product ion transitions were monitored in multiple reaction monitoring (MRM) mode: *m*/*z* 501.2→355.1 (Baohuoside II), *m*/*z* 477.0→284.9 (CAG), *m*/*z* 431.0→269.0 (ON), *m*/*z* 284.9→253.0 (CA), *m*/*z* 269.0→237.0 (FMN).

2.14.2 HPLC analysis

For solubility, stability, PAMPA, and SPIP experiments, samples were treated with methanol, subjected to centrifugation at 13,000 rpm for 10 min, and then the supernatants were collected. For bidirectional transport experiments, each 100 μL sample was mixed with 20 μL of IS solution (Baohuoside I, 6.25 μg/mL in methanol) and 380 μL of methanol. The mixtures were subjected to ultrasonic extraction (40 kHz, 25 ℃) for 30 min, followed by centrifugation at 13,000 rpm for 10 min. The resulting supernatants were carefully collected. All supernatants were filtered through 0.22 μm membranes before HPLC analysis.

HPLC analysis was performed on a Waters Alliance E2695 system equipped with a Waters 2489 UV/Vis detector. Samples were separated on a Waters XBridge HPLC C_{18} column (4.6 × 150 mm, 5 μm) at a flow rate of 0.8 mL/min. Detection was carried out at 254 nm, with the column temperature maintained at 30 ℃. The mobile phase consisted of water (A) and acetonitrile (B) under the following gradient elution program: 0–2 min, 20%–23% B; 2–4 min, 23%–24% B; 4–5 min, 24% B; 5–7 min, 24%–25% B; 7–12 min, 25%–35% B; 12–18 min, 35%–100% B.

2.15 Statistical analysis

All graphical representations were generated using Origin 2021 software (OriginLab Corporation, USA). Data are expressed as mean ± standard deviation (mean ± SD). Statistical analyses were performed using SPSS 26.0 (IBM Corporation, USA). Comparisons between two independent groups were conducted using unpaired Student's t-tests. For multiple group comparisons, one-way analysis of variance (ANOVA) was employed, followed by Dunnett's post hoc test. A probability value of $P < 0.05$ was considered statistically significant.

3. Results

3.1 Effects of honey on the oral bioavailability of AFs

The mean plasma concentration-time curves of CAG, ON, CA, and FMN are shown in Fig. 1, with absorption and metabolism parameters summarized in Table 1. AFs exhibited T_{max} within 0.5 h and $t_{1/2}$ less than 2 h, indicating their rapid absorption, distribution, and metabolism *in vivo*. Notably, CAG and CA displayed distinct double-peak phenomena in their plasma concentration-time profiles, likely attributable to enterohepatic recirculation[23,24]. Compared to the AFs group, the AFs-honey group demonstrated significantly increased AUC_{0-t} (1.8–5.9-fold) for all four flavonoids and higher C_{max} (1.9–5.1-fold) for CAG, ON, and CA. These findings suggest that honey can effectively improve the oral bioavailability of AFs. Additionally, the validation results for selectivity, calibration curve, lower limit of quantification (LLOQ), precision, accuracy, stability, matrix effect and recovery are presented in Fig. S1 and Table S1–S4.

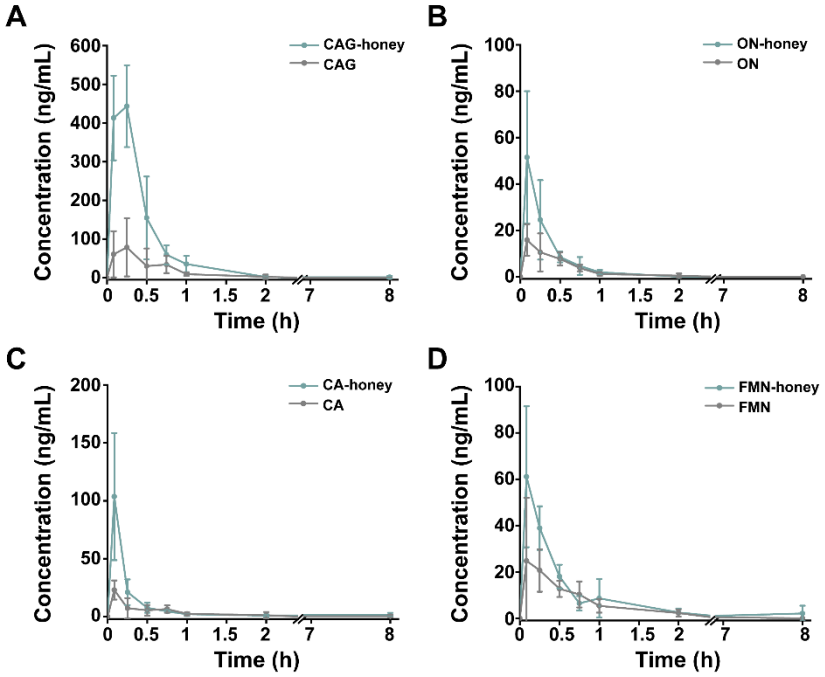

Fig. 1. Mean plasma concentration-time curves of CAG (A), ON (B), CA (C), and FMN (D) in SD rats after oral administration of AFs alone or combined with honey. All data are presented as mean ± SD (n = 6).

Table 1 Main absorption and metabolism parameters after oral administration of AFs alone or combined with honey (n = 6).

Groups	AUC_{0-t} (ng/mL·h)	$AUC_{0-\infty}$ (ng/mL·h)	MRT_{0-t} (h)	$t_{1/2}$ (h)	T_{max} (h)	C_{max} (ng/mL)
CAG	43.073 ± 29.724	46.216 ± 30.462	0.482 ± 0.207	0.343 ± 0.156	0.389 ± 0.287	97.283 ± 58.901
CAG-honey	254.741 ± 61.695***	255.606 ± 61.429***	0.622 ± 0.228	0.610 ± 0.445	0.167 ± 0.091	498.650 ± 68.859***
ON	7.457 ± 2.588	8.401 ± 3.124	0.408 ± 0.119	0.405 ± 0.293	0.222 ± 0.215	16.204 ± 6.413
ON-honey	15.030 ± 4.726**	15.686 ± 4.407**	0.272 ± 0.069	0.222 ± 0.159	0.111 ± 0.068	55.924 ± 23.447**
CA	12.779 ± 7.977	18.865 ± 12.346	1.312 ± 1.149	1.471 ± 2.151	0.083 ± 0.000	23.040 ± 8.236
CA-honey	30.477 ± 5.930**	38.407 ± 6.791**	1.689 ± 0.580	3.796 ± 4.014	0.083 ± 0.000	103.611 ± 54.854*
FMN	21.191 ± 7.396	22.230 ± 8.099	0.985 ± 0.506	0.817 ± 0.760	0.278 ± 0.245	30.164 ± 24.734
FMN-honey	38.057 ± 10.626*	39.786 ± 10.175**	1.414 ± 0.448	1.581 ± 0.475	0.264 ± 0.367	62.060 ± 29.024

*P < 0.05, **P < 0.01, and ***P < 0.001 vs the AFs group

3.2 Self-assembly properties of honey

The Tyndall effect was observed in aqueous solution of honey, indicating the presence of nanoscale aggregates (Fig. 2A). TEM images revealed that the constituents of honey self-assembled into unique chain-like aggregates in aqueous solution, in which sugar molecules likely function as the structural scaffold, while other constituents stabilize the overall structure via intermolecular interactions (Fig. 2B). Further analysis determined that the CAC of honey is 1.83 mg/mL. When the honey concentration exceeded the CAC, fluorescence probes became extensively encapsulated within the hydrophobic microdomains of the aggregates, resulting in a distinct transition zone. This indicates that hydrophobic interactions constitute the primary driving force for the self-assembly of honey in aqueous solution (Fig. 2C).

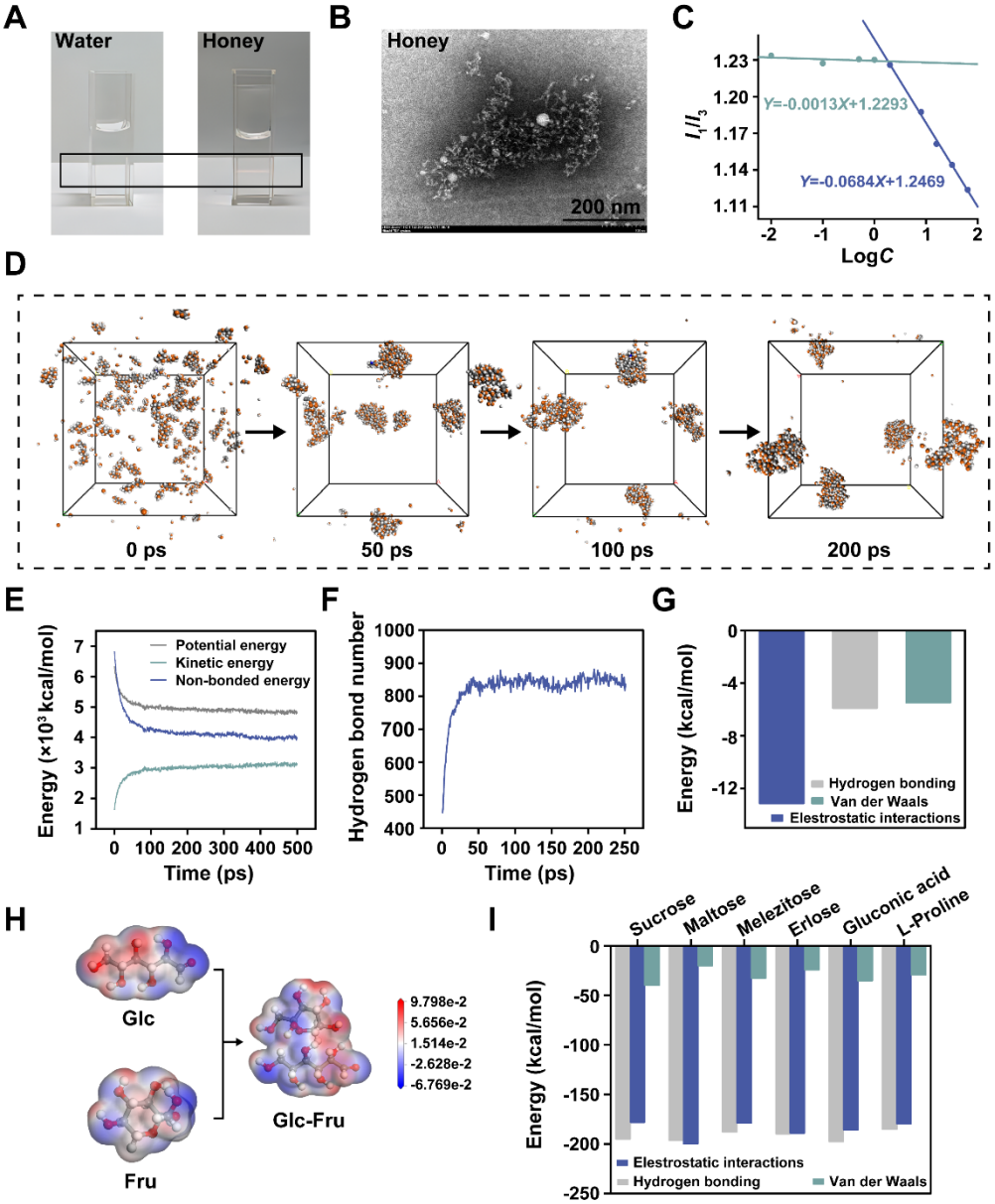

Fig. 2. Self-assembly properties of honey. (A) Tyndall phenomenon of honey in aqueous solution. (B) TEM images of honey. (C) The CAC of honey. (D) Snapshots of the MD simulation from 0 to 200 ps. (E) Changes in non-bonded energy, potential energy, and kinetic energy in MD simulation systems. (F) Changes in the number of hydrogen bonds in MD simulation systems. (G) Analysis of interactions between glucose and fructose. (H) Molecular electrostatic potential surfaces analysis of glucose, fructose, and their binary system. (I) Analysis of interactions between the glucose-fructose binary system and other representative constituents.

Based on prior analysis of honey's chemical composition, eight representative constituents were selected for MD simulations: glucose, fructose, sucrose, maltose, melezitose, erlose, gluconic acid, and L-proline[25-28]. The system composition was defined as 12% H_2O, 70% monosaccharides, 16% oligosaccharides, and 2% other constituents. As shown in Fig. 2D, the molecules were randomly distributed in aqueous solution at 0 ps. By 50 ps, nascent molecule clusters had formed. Finally, at 100 ps, all molecules self-assembled into stable aggregates, with convergent structural stability observed thereafter. The simulation data indicated that both the non-bonded energy and potential energy decreased throughout the simulation, suggesting that a gradual weakening of van der Waals forces and the increasing dominance of hydrogen bonds as the primary stabilizing force during the self-assembly process (Fig. 2E). This redistribution of intermolecular interactions facilitated the formation of more stable molecular aggregates. Additionally, as the self-assembly process proceeded, the number of hydrogen bonds gradually increased and reached a dynamic equilibrium after 50 ps, further confirming the significant role of hydrogen bonding in the self-assembly of honey (Fig. 2F). Glucose and fructose, as the predominant saccharides in honey, play a crucial role in the formation of honey's supramolecular structure through both their intermolecular interactions and their interactions with other constituents. Computational analysis demonstrated that the molecular interactions between glucose and fructose were predominantly electrostatic interactions, whereas the interactions between the glucose-fructose binary system and other representative constituents were primarily governed by hydrogen bonding and electrostatic interactions (Fig. 2G-I). In summary, the constituents of honey can self-assemble through non-covalent interactions such as hydrogen bonding, van der Waals forces, electrostatic interactions and hydrophobic interactions, forming a stable supramolecular structure.

3.3 Molecular interactions between honey and AFs

3.3.1 Multiscale structural analysis of the AFs-honey aggregates

The DLS results demonstrated a significant increase in particle size with incremental addition of honey, indicating the occurrence of molecular aggregation between AFs and honey in aqueous solution (Fig. 3A). The PDI remained consistently below 0.2 throughout the experiments, suggesting good monodispersity of the formed aggregates (Fig. 3B and 3D). Notably, while the absolute value of ζ potential exhibited a slight decrease, it maintained relative stability during the entire process (Fig. 3C). These findings collectively suggest that AFs and honey form uniform and stable aggregates through intermolecular interactions, with the average particle size of these aggregates being larger than that of AFs alone. Moreover, the CAC of the AFs-honey aggregates was determined to be 0.17 mg/mL, significantly lower than that of honey (Fig. S2). This indicates that the intermolecular interactions between AFs and honey enhance the system's aggregation propensity, promoting stable aggregate formation at reduced concentrations.

The morphology of the samples was characterized by TEM, with representative images shown in Fig. 3E. The AFs appeared as monodisperse spherical particles with diameters less than 100 nm. The observed particle sizes differed from DLS measurements due to nanoparticle swelling in aqueous solution and shrinkage during TEM sample preparation. When interacting with honey, the AFs became embedded within the porous

structure of honey or were encapsulated by honey via intermolecular interactions, forming tightly structured aggregates. The SEM images further revealed the surface morphology of the samples (Fig. 3F). Honey possessed a relatively large specific surface area with uneven microstructures, which enhanced the contact between AFs and honey, providing multiple embedding sites for AFs. The AFs-honey aggregates exhibited a distinctly porous structure, with flake-like AFs either adsorbed onto the honey surface or embedded within its cavities.

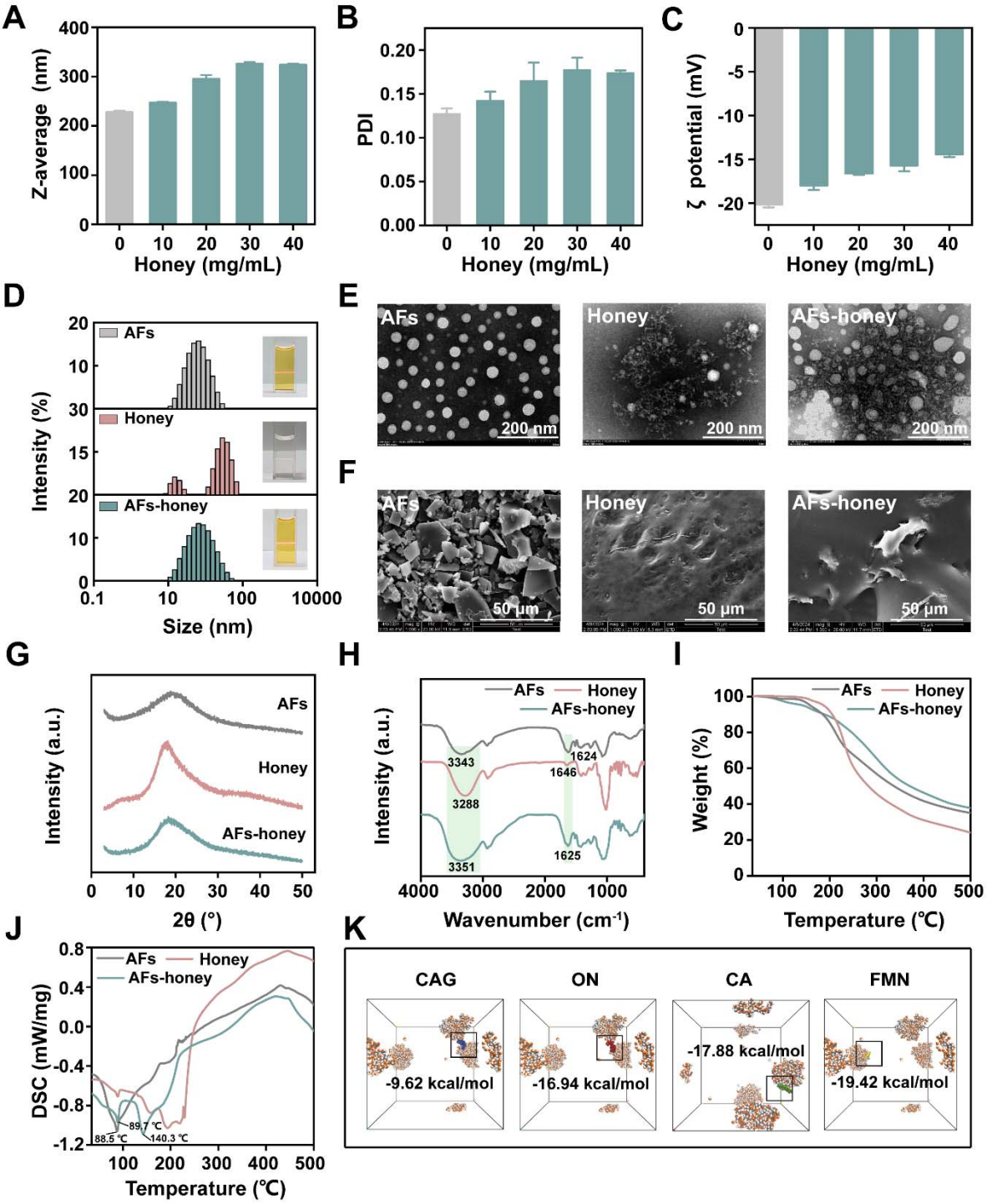

Fig. 3. Characterization of AFs-honey aggregates and their formation mechanism. (A–C) The z-average, PDI, and ζ potential of AFs-honey aggregates. (D) Particle size distributions. (E) TEM images. (F) SEM images. (G) XRD patterns. (H) FT-IR spectra. (I) TG curves. (J) DSC curves. (K) Calculated interaction energies between AFs and honey.

3.3.2 Formation mechanism of AFs-honey aggregates

XRD analysis was used to characterize the structural properties of AFs, honey and AFs-honey aggregates (Fig. 3G). Crystalline substances typically exhibit sharp and well-defined diffraction peaks in XRD patterns, whereas amorphous substances display broad halos or nearly featureless patterns[29]. The XRD patterns of both AFs and honey showed a broad halo centered at approximately 20° without distinct diffraction peaks, indicating their amorphous nature. This structural feature is related to multiple functional groups (hydrogen bond donors and acceptors) in AFs and honey, which form intricate intramolecular and intermolecular hydrogen-bonding networks. Compared to AFs alone, the XRD pattern of the aggregates showed no significant changes, indicating that no new crystalline structures were formed between AFs and honey, nor were significant structural alterations observed.

To further investigate the intermolecular interactions between AFs and honey, FT-IR analysis was performed. As shown in Fig. 3H, compared with AFs and honey alone, no novel absorption peaks were observed in the FT-IR spectrum of the AFs-honey aggregates, indicating their interactions were primarily physical rather than covalent bond formation. Previous studies have established that AFs can self-assemble into nanoparticles via intermolecular hydrogen bonding and π-π stacking interactions, manifested by the broad and intense O-H stretching vibration at 3343 cm^{-1}[30]. Upon honey addition, competitive hydrogen bonding occurred between AFs and honey constituents, resulting in a blue-shift of the O-H stretching vibration (from 3343 cm^{-1} to 3351 cm^{-1}). Additionally, the C=O stretching vibration of honey exhibited a red-shift (from 1646 cm^{-1} to 1625 cm^{-1}), demonstrating non-covalent interactions between the polar termini of honey constituents and the conjugated aromatic structure of AFs.

Furthermore, the thermal stability and behavior of AFs, honey, and AFs-honey aggregates were analyzed by TGA and DSC. TG analysis revealed that AFs underwent 65.10% mass loss over 35–500 ℃, while AFs-honey aggregates showed a mass loss of 62.23% over the same temperature range. This demonstrates that AFs-honey aggregates possess enhanced thermal stability with slower decomposition kinetics compared to AFs alone (Fig. 3I). Notably, while the DSC curve of AFs showed a single endothermic peak at 88.5 ℃, the AFs-honey aggregates displayed two distinct endothermic peaks at 89.7 ℃ and 143.0 ℃. These changes in thermal behavior indicate that AFs-honey aggregates are stabilized by specific non-covalent interactions, rather than mere physical mixing (Fig. 3J).

As shown in Fig. 3K, MD simulations demonstrated that flavonoid aglycones bind more strongly to honey than their glycosylated counterparts. Notably, FMN exhibited the highest binding affinity, with a binding energy of -19.42 kcal/mol, while CAG displayed the lowest binding affinity, which resulted in a binding energy of merely -9.62 kcal/mol. This difference likely stems from the steric hindrance of glycosyl groups, competitive hydrogen bonding, and reduced hydrophobic interactions.

3.4 Effects of honey on the equilibrium solubility of AFs

The absorption of bioactive constituents in the gastrointestinal tract is highly dependent on solubility[31-33]. In this study, the equilibrium solubility of AFs was determined to compare their solubility in

honey aqueous solution versus pure water. As shown in Fig. 4A and Fig. S3, the presence of honey increased the solubility of CAG, ON, CA, and FMN by 1.17-, 1.19-, 1.20-, and 1.21-fold, respectively. These results suggest that AFs form aggregates with honey through intermolecular interactions, thereby enhancing their solubility.

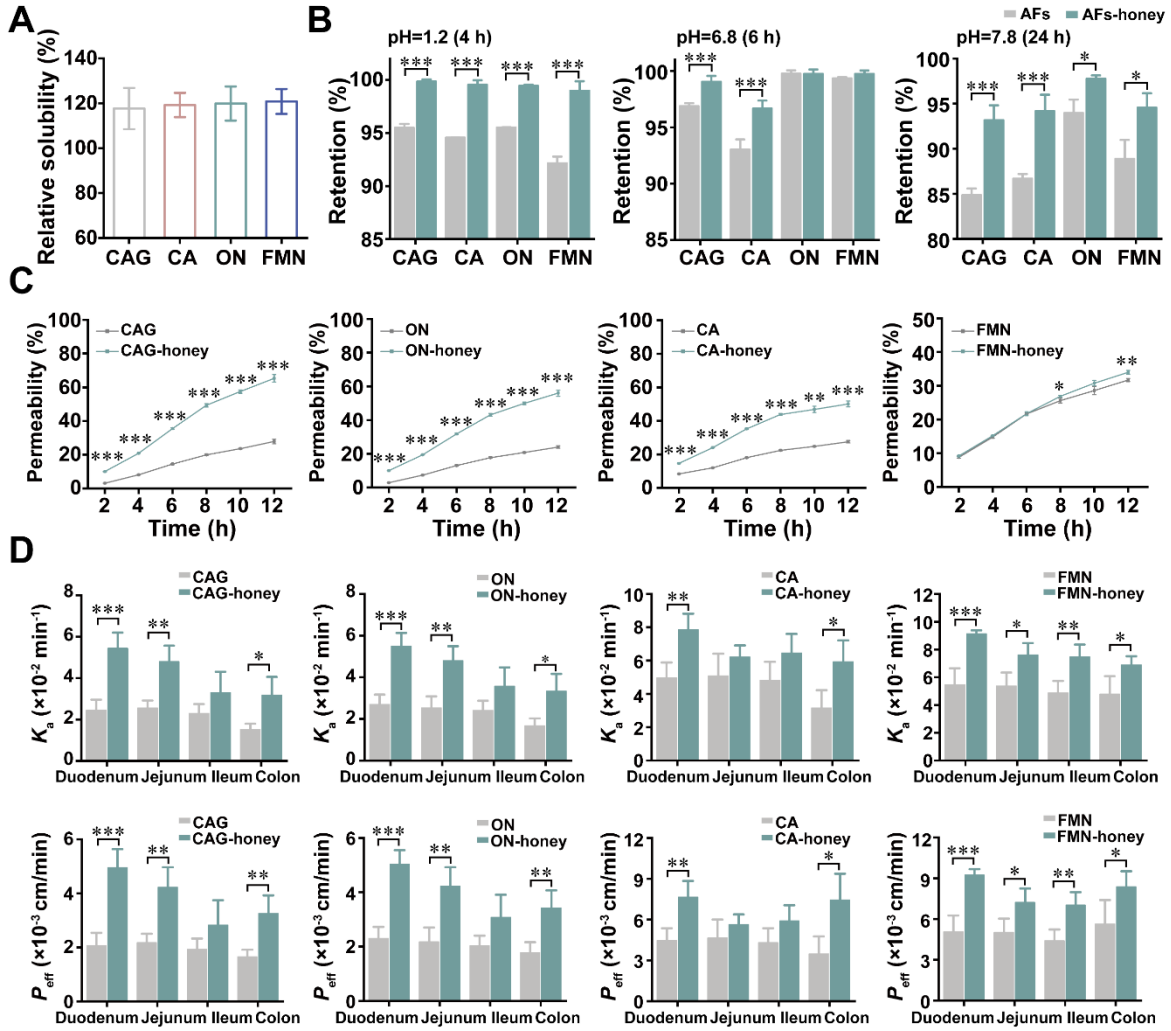

Fig. 4. Effects of honey on solubility, gastrointestinal stability, permeability, and intestinal absorption potential of AFs. (A–C) Effects of honey on the solubility, gastrointestinal stability, and permeability of AFs. Data are presented as mean ± SD (n = 3). $^{*}P < 0.05$, $^{**}P < 0.01$, and $^{***}P < 0.001$ vs the AFs group. (D) The K_a and P_{eff} measured by SPIP. Data are presented as mean ± SD (n = 4). $^{*}P < 0.05$, $^{**}P < 0.01$, and $^{***}P < 0.001$ vs the AFs group.

3.5 Effects of honey on the stability of AFs in simulated gastrointestinal fluids

The stability of bioactive constituents in the gastrointestinal tract is a critical determinant of blood absorption[34,35]. We evaluated the protective effects of honey on the gastrointestinal stability of AFs by measuring their retention rates after incubation in artificial digestive fluids for physiologically relevant durations. As shown in Fig. 4B, the retention rates of CAG, ON, CA, and FMN exceeded 80% in the simulated gastric, intestinal, and colonic fluids, indicating their favorable stability in the simulated gastrointestinal environment. The addition of honey further enhanced the stability of AFs, which may have a positive influence on their gastrointestinal absorption. These protective effects may be attributable to the formation of AFs-honey aggregates via non-covalent interactions. These aggregates provide a physical barrier that

effectively shields the flavonoids from digestive enzymes, acidic conditions, and other degradation-promoting factors in the gastrointestinal fluids, consequently slowing their degradation. Additionally, the viscosity of honey contributes to the formation of structurally stable aggregates. This not only helps maintain the molecular structure of AFs, but also further minimizes their susceptibility to environmental factors.

3.6 Effects of honey on the permeability of AFs

The effects of honey on the *in vitro* permeability of AFs were dynamically evaluated using the PAMPA model, as illustrated in Fig. 4C. After honey treatment, significantly increased concentrations of CAG, ON, CA, and FMN were detected at different time points, indicating that honey can enhance the permeation of AFs across the artificial membrane. The underlying mechanisms may involve alterations in the fluidity of the artificial membrane or the formation of AFs-honey aggregates through interactions. Interestingly, the permeability of ON (24.00%) was lower than that of its corresponding aglycone–FMN (31.69%), and honey exhibited a more pronounced promoting effect on the permeability of glycosides compared to aglycones. These results suggest that honey possesses the potential to enhance the permeability of AFs to some extent, which may facilitate their intestinal absorption.

3.7 Effects of honey on the intestinal absorption of AFs

The SPIP experiment was used to investigate the effects of honey on the intestinal absorption of AFs (Fig. 4D). The P_{eff} serves as a quantitative measure of absorption potential in this model. A $P_{eff} > 1.2 \times 10^{-3}$ cm·min^{-1} denotes high intestinal permeability, suggesting that bioactive molecules can easily cross the intestinal wall and enter systemic circulation[36-38]. Conversely, a $P_{eff} < 0.18 \times 10^{-3}$ cm·min^{-1} indicates low intestinal permeability and poor absorption potential. CAG, CA, ON, and FMN all showed $P_{eff} > 1.2 \times 10^{-3}$ cm·min^{-1} in the duodenum, jejunum, ileum, and colon, demonstrating favorable absorption potential. Notably, their absorption potential was stronger in the small intestine than in the colon, likely attributable to the larger absorptive surface area provided by the extensive villi and microvilli in the small intestine, as well as the denser epithelial cellular architecture. Furthermore, a marked difference was observed between aglycones and glycosides, with the former showing significantly higher *in vivo* permeability and absorption rates, consistent with their greater lipophilicity enhancing cell membrane traversal. Interestingly, AFs exhibited enhanced intestinal permeability and absorption potential after co-treatment with honey, with the most pronounced effect observed in the duodenum. These findings can be explained by solubility enhancement via the formation of AFs-honey aggregates, membrane fluidization-induced permeability augmentation, and prolonged intestinal residence time attributable to honey's viscosity.

3.8 Establishment and characterization of Caco-2 cell monolayer model

Caco-2 cells have been widely used in intestinal absorption and transport studies of bioactive constituents due to their ability to differentiate into polarized epithelial monolayers and recapitulate intestinal physiology, including brush border enzyme expression and tight junction barrier function. The integrity and tightness of Caco-2 cell monolayer model must be rigorously evaluated. TEER values are a critical indicator of tight junction integrity, reflecting ionic flux through the paracellular pathway. As shown in Fig. S4A, the TEER

values progressively increased and finally stabilized at approximately 690 Ω·cm² on the 21st day, demonstrating good monolayer integrity. Alkaline phosphatase (ALP), a brush border marker enzyme, serves as an indicator of both cellular differentiation status and membrane polarity. By 21 days, the ALP activity (AP/BL ratio) reached 5.45, revealing that Caco-2 cells have achieved functional differentiation and established mature epithelial polarity (Fig. S4B). In addition, the SEM and TEM images showed dense microvilli on cell surface and distinct tight junctions between adjacent cells (Fig. S4C). The above results confirmed that the established Caco-2 cell monolayer model exhibited good barrier integrity, mature tight junctions, and functional polarization, fulfilling the requirements for subsequent studies.

3.9 Effects of honey on the bidirectional transport of AFs across Caco-2 cell monolayers

To investigate the effects of honey on the bidirectional transport of AFs, the working concentrations of honey and AFs were first determined through cytotoxicity assessment using CCK-8 assays (Fig. S5). Following a 24 h exposure to AFs (0–800 μg/mL) or honey (0–32 mg/mL), Caco-2 cell viability remained above 90%, demonstrating absence of significant cytotoxicity at these concentrations. Based on cytotoxicity assessment of AFs and honey co-treatment, we selected 800 μg/mL AFs and 20 mg/mL honey for further experiments.

According to Fig. 5A-B and Table S5, the P_{app}(AP→BL) values of CA and FMN were significantly higher than those of CAG and ON, consistent with deglycosylation-induced molecular weight reduction and lipophilicity enhancement. Furthermore, the ER values of ON, CA, and FMN all exceeded 2.0, indicating their transport may be regulated by efflux transporters. In contrast, CAG exhibited a lower ER value of 1.24, suggesting passive diffusion as its predominant transport mechanism, although potential involvement of efflux transporters cannot be completely ruled out. Following honey treatment, CAG, CA, ON, and FMN showed significantly higher P_{app}(AP→BL), unchanged P_{app}(BL→AP), and reduced ER values. The reduction in ER values was attributed to enhanced net absorption efficiency. These data indicate that honey significantly promotes the transmembrane absorption of AFs, likely through pathways other than efflux transporter inhibition. P-gp, MRP2, and BCRP are efflux transporters that actively pump bioactive constituents from intestinal epithelial cells back into the lumen, thereby reducing drug bioavailability. Accumulating evidence demonstrates that these three proteins serve as major efflux transporters for flavonoids[39-41]. As shown in Fig. 5C-F, the P_{app}(AP→BL) values of CAG, CA, ON, and FMN significantly increased in the presence of specific efflux transporter inhibitors: verapamil, probenecid, dipyridamole. These results confirm that the absorption of AFs is indeed modulated by efflux transporters. Notably, the co-treatment of honey with the inhibitor resulted in an increase in P_{app}(AP→BL) value compared to the inhibitor alone, further indicating that honey's effects on the transmembrane transport of AFs are not primarily due to the inhibition of efflux transporter activity, but rather through alternative mechanisms, such as transient modulation of tight junction permeability.

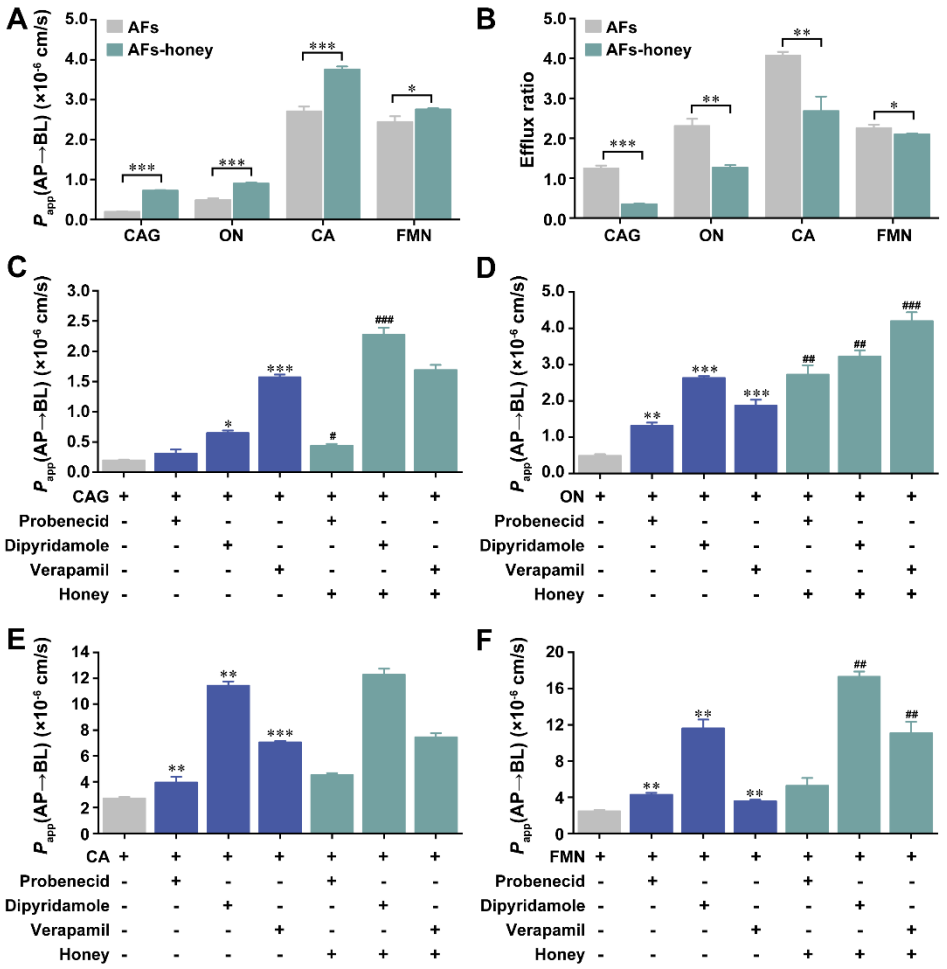

Fig. 5. Effects of honey on the bidirectional permeability of AFs across Caco-2 cell monolayers. (A) The P_{app}(AP→BL) of CAG, ON, CA, and FMN with or without honey co-treatment. (B) The ER of CAG, ON, CA, and FMN with or without honey co-treatment. (C–F) Effects of different efflux protein inhibitors (verapamil, probenecid, and dipyridamole) and their combinations with honey on the P_{app}(AP→BL) of CAG, ON, CA, and FMN. Data are presented as mean ± SD (n = 3). $^{*}P < 0.05$, $^{**}P < 0.01$, and $^{***}P < 0.001$ vs the AFs group; $^{\#}P < 0.05$, $^{\#\#}P < 0.01$ and, $^{\#\#\#}P < 0.001$ vs the inhibitors group.

3.10 Effects of honey on tight junction barrier in Caco-2 cells

The P_{app}(AP→BL) of sodium fluorescein was calculated below 5.0 × 10^{-7} cm·s^{-1}, indicating the formation of an intact cell monolayer capable of effectively preventing marker permeation and reliably simulating intestinal barrier function[42] (Fig. 6A). Paracellular permeability exhibits an inverse correlation with TEER values, making TEER values serve as a reliable metric for assessing tight junction integrity[43,44]. As displayed in Fig. 6B, TEER values decreased significantly by approximately 27.74% after treatment with 20 mg/mL honey for 2 h. After the removal of honey intervention, TEER values returned to baseline levels within 24 h. Furthermore, the cell viability remained above 90% at this honey experimental dose, demonstrating that the TEER changes were not due to cytotoxicity. These results suggest that honey reversibly opens tight junctions, enhancing paracellular transport. Occludin and claudin-1, as the key transmembrane proteins of tight junctions, play crucial roles in dynamic regulation and structural integrity, respectively. Specifically, occludin dynamically modulates the stability of the tight junction barrier through signal transduction and interaction with the scaffold protein ZO-1, whereas claudin-1 directly forms the intercellular "sealing strands" that govern the selective permeability of tight junctions[45-47]. ZO-1, as the core scaffold

protein of tight junctions, maintains the structural integrity of tight junctions by linking transmembrane proteins to the cytoskeleton[48]. Additionally, although the cell adhesion protein β-catenin, located on the basolateral side of tight junctions, primarily participates in intercellular adhesion, it collaborates with tight junction proteins to collectively maintain the integrity and functionality of the epithelial barrier[49]. CLSM results demonstrated that before honey treatment, β-catenin, occludin, claudin-1, and ZO-1 exhibited continuous and smooth circumferential distribution between adjacent cells with high fluorescence intensity, indicating intact structures of both tight junctions and adherens junctions. However, at 2 h after honey treatment, the fluorescence intensity of these proteins was significantly attenuated, with intercellular connections appearing blurred, discontinuous, or even locally absent, suggesting structural disruption of tight junctions. Notably, upon honey removal, both cellular morphology and tight junction distribution recovered to near-initial states, which correlated well with changes in TEER values (Fig. 6C). These findings further demonstrate that honey reversibly modulates tight junction barrier function. In summary, honey transiently disrupts intercellular junctions by interfering with the assembly or stability of tight junction proteins, and these effects are reversible upon stimulus removal. The concomitant attenuation of β-catenin signal suggests that honey may simultaneously affect the synergistic interaction between adherens junctions and tight junctions.

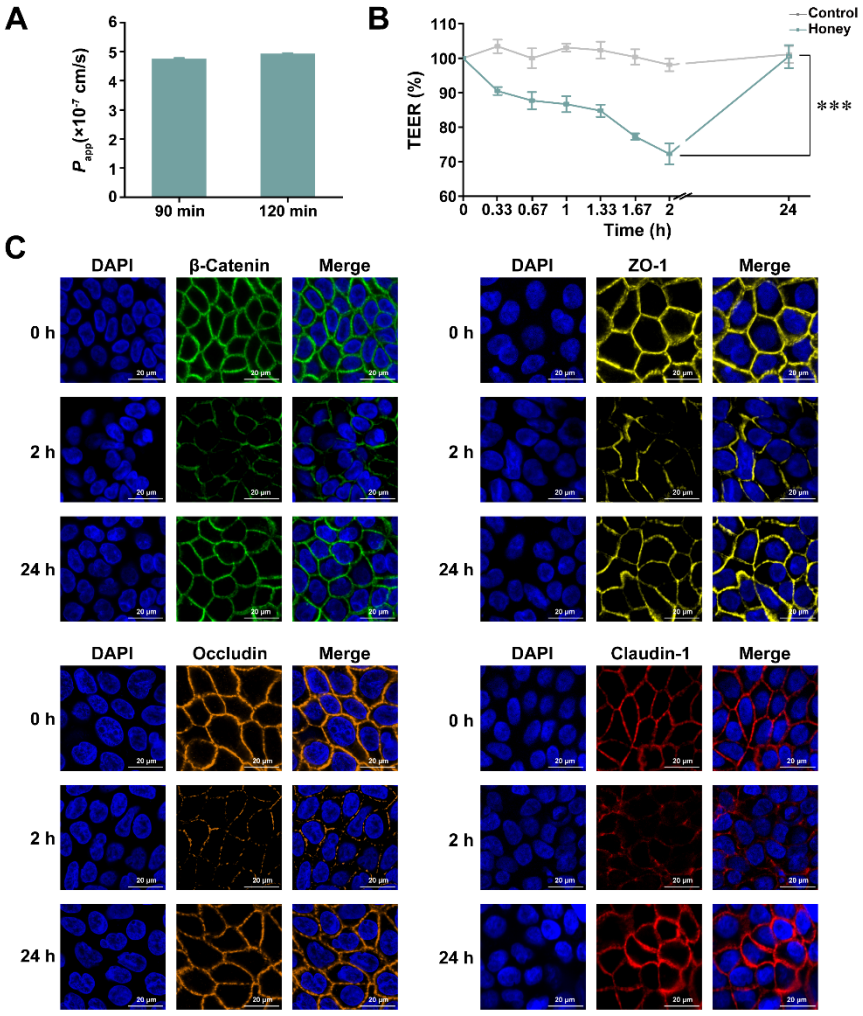

Fig. 6. Effects of honey on tight junction barrier. (A) The P_{app}(AP→BL) of sodium fluorescein. (B) TEER changes in cell monolayers (normalized to initial values). (C) CLSM images of β-catenin, ZO-1, occludin and claudin-1. Scale bar: 20 μm. Data are presented as the mean ± SD (n = 3). $^{***}P < 0.001$ vs the control group.

3.11 Effects of honey on the Qi-tonifying efficacy of AFs

3.11.1 Effects on SI

The SI serves as a quantitative indicator of immune response intensity and the functional status of the immune system in nude mice. Following intrapulmonary tumor cell inoculation, alterations in the tumor microenvironment can lead to the suppression or even exhaustion of immune cell activity, resulting in a decline in overall splenic function. As shown in Fig. S6, the SI in the model group was significantly lower than that in the control group ($P < 0.01$). Compared with the model group, the SI in the CDDP group exhibited a decreasing trend, likely attributable to the pronounced immunosuppressive effects of CDDP, which directly inhibits lymphocyte proliferation. Moreover, the cytotoxicity of CDDP is not limited to tumor cells but also induces damage and apoptosis in normal cells[50,51]. In contrast, the SI was significantly elevated in the BFP ($P < 0.001$), AFs-H ($P < 0.05$), and AFs-honey-H ($P < 0.001$) groups, suggesting that both BFP and AFs possess immunoenhancing activity. Notably, the SI in the AFs-honey-H group was significantly higher than that in the AFs-H group ($P < 0.05$), indicating that the combination of honey and AFs further enhances splenic immune function.

3.11.2 Effects on pulmonary function

As illustrated in Fig. 7B, nude mice in the model group exhibited significant respiratory abnormalities, including tachypnea, elevated airway resistance, and compromised gas exchange efficiency, due to pulmonary tumor progression. This ultimately resulted in significant pulmonary dysfunction, characterized by markedly decreased PEF, PIF, TV, and EF50 values ($P < 0.001$), along with significantly increased f and PenH values ($P < 0.001$). Comparative analysis revealed that neither the CDDP group nor the honey group exhibited substantial improvement in any pulmonary parameters relative to the model group, suggesting potential irreversible tissue damage induced by CDDP chemotherapy and limited honey efficacy in pulmonary function enhancement. In contrast, all other treatment groups demonstrated statistically significant improvements in pulmonary function parameters. Particularly noteworthy was the superior efficacy of AFs-honey combination therapy compared to AFs monotherapy at equivalent doses, as evidenced by significant enhancements in f, PEF, PIF, EF50, and PenH parameters ($P < 0.05$ or $P < 0.01$). These findings suggest that honey potentiates the bioactivity of AFs through improved absorption, thereby resulting in synergistic therapeutic effects.

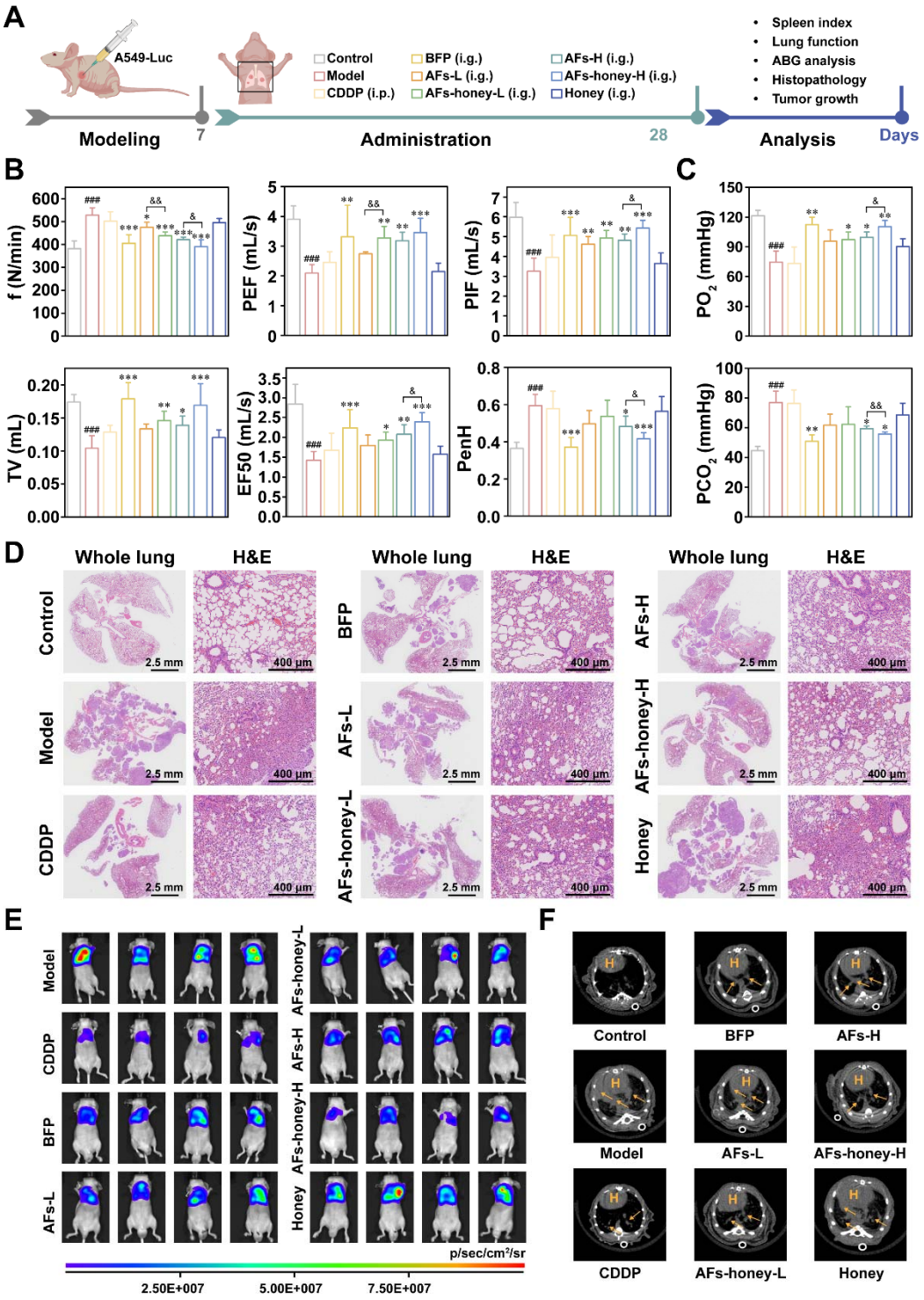

Fig. 7. Combined therapy of honey and AFs for lung Qi Deficiency syndrome. (A) Treatment schedule for therapy. (B) Fundamental parameters of pulmonary function. (C) PO_2 and PCO_2 in arterial blood. (D) H&E-stained sections of lung tissue. (E) IVIS-images of pulmonary tumors. (F) Micro-CT images of pulmonary tumors (H: Heart; arrows: tumor mass). Scale bar: 2.5 mm and 400 μm. Data are presented as mean ± SD ($n = 6$). $^{###}P < 0.001$ vs the control group; $^{*}P < 0.05$, $^{**}P < 0.01$, and $^{***}P < 0.001$ vs the model group; $^{\&}P < 0.05$ and $^{\&\&}P < 0.01$ vs the same dose of AFs alone group.

3.11.3 Effects on PO2 and PCO2 in arterial blood

As illustrated in Fig. 7C, compared with the control group, nude mice in the model group exhibited significantly decreased PO_2 and increased PCO_2 ($P < 0.001$), indicating impaired pulmonary gas exchange secondary to tumor progression, which led to hypoxemia and metabolic waste accumulation. Therapeutic intervention analysis revealed that the BFP, AFs-H, and AFs-honey-H groups all demonstrated significant

improvements in pulmonary function parameters compared to the Model group, with elevated PO_2 ($P < 0.01$, $P < 0.05$, and $P < 0.01$, respectively) and reduced PCO_2 ($P < 0.01$, $P < 0.05$, and $P < 0.05$, respectively). These data suggest that these treatments effectively enhance alveolar gas exchange, facilitating oxygen uptake and CO_2 elimination, thereby ameliorating respiratory insufficiency and restoring metabolic homeostasis. Notably, the AFs-honey-H group showed superior therapeutic outcomes compared to the AFs-H group, with higher PO_2 values ($P < 0.05$) and lower PCO_2 levels ($P < 0.01$), demonstrating honey's effects on enhancing the therapeutic efficacy of AFs.

3.11.4 Effects on pulmonary histopathology

Following euthanasia, intact lung tissues were harvested from nude mice, revealing translucent, smooth-surfaced tumor nodules on the pulmonary surface. Comparative analysis demonstrated varying degrees of reduction in both tumor number and size across all treatment groups except the honey group when compared to the model group, with the most pronounced effects observed in the CDDP, BFP, and AFs-honey-H groups (Fig. S7). Histopathological examination by H&E staining (Fig. 7D) showed well-preserved pulmonary architecture of nude mice in the control group, whereas the lung tissues in the model group exhibited significant pathological alterations, including neoplastic cell proliferation, alveolar atrophy, and inflammatory cell infiltration. While the honey group showed no significant improvement in pulmonary histopathology compared to the model group, all other treatment groups displayed differential degrees of improvement in pathological conditions. Notably, the AFs-honey combination therapy conferred superior pulmonary protection compared to AFs monotherapy.

3.11.5 Effects on pulmonary tumor growth

In vivo imaging analysis results (Fig. 7E and Fig. S8) demonstrated that the CDDP group exhibited the lowest fluorescence intensity, with statistically significant differences compared to the model group ($P < 0.001$). This indicates that CDDP effectively inhibited pulmonary tumor growth in nude mice. Furthermore, compared to the model group, significant reductions in pulmonary tumor fluorescence intensity were observed in all treatment groups except for the honey group ($P < 0.01$ or $P < 0.001$). These findings suggest that both BFP and AFs enhance the body's vital energy, improve immune competence, and reinforce physiological resistance against pathological factors, thereby suppressing pulmonary tumor progression. Notably, the combination therapy of AFs (36 mg/kg) with honey (900 mg/kg) resulted in significantly lower tumor fluorescence intensity than AFs monotherapy at the same dose ($P < 0.05$), indicating that honey enhances the bioavailability and therapeutic efficacy of AFs. These experimental results were further validated by micro-CT scanning of nude mouse lungs (Fig. 7F and Fig. S9), which provided additional morphological evidence of tumor growth inhibition across treatment groups.

4. Conclusion

This study systematically investigated the absorption-enhancing effects of honey on AFs and the underlying mechanisms. The findings demonstrated that saccharides, organic acids, and amino acids in honey

could self-assemble into chain-like supramolecular structures in aqueous solutions through non-covalent interactions, including hydrogen bonding, van der Waals forces, electrostatic interactions, and hydrophobic effects. When coexisting with honey, AFs could either embed into the nanopores of honey's supramolecular structure or be encapsulated, forming aggregates that significantly improved the solubility, stability in simulated gastrointestinal fluids, and *in vitro*/*in vivo* permeability of AFs. Mechanistic studies revealed that honey reversibly modulated intestinal epithelial tight junction proteins, transiently opening the paracellular pathways to facilitate the paracellular permeability of AFs. These effects ultimately enhanced intestinal absorption of AFs, leading to increased systemic exposure and improved oral bioavailability.

Although this study provides both theoretical foundations and practical references for developing honey as a natural absorption enhancer, the differences in chemical composition and physicochemical properties of honey due to its botanical origin (e.g., floral source) may influence its absorption-enhancing efficacy. Furthermore, whether these enhancement effects exhibit universal applicability to other bioactive components requires further investigation. Additionally, the interaction between honey and key absorption barriers–including physical barriers (e.g., intestinal mucus layer) and biological barriers (e.g., gut microbiota)–warrants in-depth exploration to fully elucidate the absorption enhancement mechanisms.

Declaration of Competing Interest

The authors declare that they have no known competing financial interests or personal relationships that could have appeared to influence the work reported in this paper.

Acknowledgements

This work was supported by the National Natural Science Foundation of China (No. 82204626), Jiangsu Funding Program for Excellent Postdoctoral Talent (No. 2022ZB317), and 2024 Qinglan Project Candidate for Universities and Colleges in Jiangsu (Jiangsu Provincial Department of Education Talent Program).

Appendix A. Supplementary Material

Supplementary data to this article can be found online.

Data availability

Data will be made available on request.

References

[1] Z. Chen, L. Liu, C. Gao, et al., *Astragali Radix* (Huangqi): A promising edible immunomodulatory herbal medicine, J. Ethnopharmacol. 258 (2020) 112895. https://doi.org/10.1016/j.jep.2020.112895.

[2] D. Sun-Waterhouse, X. Chen, Z. Liu, et al., Transformation from traditional medicine-food homology to modern food-medicine homology. Food Med. Homol. 1 (2024) 9420014. https://doi.org/10.26599/fmh.2024.9420014.

[3] B. Salehi, J.N.P. Carneiro, J.E. Rocha, et al., *Astragalus* species: Insights on its chemical composition toward pharmacological applications, Phytother. Res. 35 (2020) 2445–2476. https://doi.org/10.1002/ptr.6974.

[4] Z. Gao, G. Wang, Y. Chen, et al., Total flavonoids of *Astragalus membranaceus* protect against 1-methyl-4-phenyl-1,2,3,6-tetrahydropyridine-induced neurotoxicity in mice by inhibiting ferroptosis through

SLC7A11/GPX-4 signaling pathway, Food Sci. Hum. Wellness 13 (2024) 414–420. https://doi.org/10.26599/fshw.2022.9250035.

[5] B. Yang, Z. Xiong, M. Lin, et al., *Astragalus* polysaccharides alleviate type 1 diabetes via modulating gut microbiota in mice, Int. J. Biol. Macromol. 234 (2023) 123767. https://doi.org/10.1016/j.ijbiomac.2023.123767.

[6] C. Yang, X. Mao, J. Wu, et al., Amelioration of lung fibrosis by total flavonoids of *Astragalus* via inflammatory modulation and epithelium regeneration, Am. J. Chin. Med. 51 (2023) 373–389. https://doi.org/10.1142/s0192415x23500192.

[7] M. Chou, Y. Wong, S. Wang, et al., Potential antidepressant effects of a dietary supplement from Huáng qí and its complex in aged senescence-accelerated mouse prone-8 mice, Front. Nutr. 10 (2023) 1235780. https://doi.org/10.3389/fnut.2023.1235780.

[8] F. Wei, H. Wang, X. Li, et al., Preparation of Astragalus membranaceus–cranberry biscuits and the evaluation of physicochemical properties and antioxidant activity, J. Food Sci. Technol. 59 (2024) 3134–3141. https://doi.org/10.1111/ijfs.17057.

[9] M. Chien, C. Yang, C. Chen, Effects of physical properties and processing methods on Astragaloside IV and flavonoids content in Astragali radix, Molecules 27 (2022) 575. https://doi.org/10.3390/molecules27020575.

[10] B. Yang, N. Yang, Y. Chen, et al., An integrated strategy for effective-component discovery of *Astragali Radix* in the treatment of lung cancer, Front. Pharmacol. 11 (2021) 580978. https://doi.org/10.3389/fphar.2020.580978.

[11] Y. Chang, I. Wu, M. Sheu, et al., Formononetin defeats multidrug-resistant cancers by induction of oxidative stress and suppression of P-Glycoprotein, Int. J. Mol. Sci. 25 (2024) 8471. https://doi.org/10.3390/ijms25158471.

[12] X. Fang, J. Li, M. Zhang, et al., Pharmacokinetic investigation on the mechanism of interaction of anti-breast cancer calycosin with albumin: In vitro, Arabian J. Chem. 16 (2023) 105175. https://doi.org/10.1016/j.arabjc.2023.105175.

[13] A. Sheik, K. Kim, G.L. Varaprasad, et al., The anti-cancerous activity of adaptogenic herb *Astragalus membranaceus,* Phytomedicine 91 (2021) 153698. https://doi.org/10.1016/j.phymed.2021.153698.

[14] Y. Zhang, Z. Chen, L. Chen, et al., *Astragali radix* (Huangqi): a time-honored nourishing herbal medicine, Chin. Med. 19 (2024) 119. https://doi.org/10.1186/s13020-024-00977-z.

[15] M.A. Al-Kafaween, M. Alwahsh, A.B.M. Hilmi, et al., Physicochemical characteristics and bioactive compounds of different types of honey and their biological and therapeutic properties: a comprehensive review, Antibiotics 12 (2023) 337. https://doi.org/10.3390/antibiotics12020337.

[16] E. Majewska, B. Drużyńska, D. Derewiaka, et al., Comparison of antioxidant properties and color of selected polish honeys and manuka honey, Foods 13 (2024) 2666. https://doi.org/10.3390/foods13172666.

[17] P. Núñez-Pizarro, G. Montenegro, G. Núñez, et al., Comparative study of phenolic content and antioxidant and hepatoprotective activities of unifloral quillay tree (*Quillaja saponaria* Molina) and multifloral honeys from Chile, Plants 13 (2024) 3187. https://doi.org/10.3390/plants13223187.

[18] Y. Dai, R. Jin, R. Verpoorte, et al., Natural deep eutectic characteristics of honey improve the bioactivity and safety of traditional medicines, J. Ethnopharmacol. 250 (2019) 112460. https://doi.org/10.1016/j.jep.2019.112460.

[19] S. Kong, P. Li, R. Verpoorte, et al., Synergistic mechanism for the bioactivity fortification of licorice by honey, J. Ethnopharmacol. 289 (2022) 115048. https://doi.org/10.1016/j.jep.2022.115048.

[20] M. Li, C. Rao, X. Ye, et al., Applications for natural deep eutectic solvents in Chinese herbal medicines, Front. Pharmacol. 13 (2023) 1104096. https://doi.org/10.3389/fphar.2022.1104096.

[21] W. Zhang, J. Song, X. Su, et al., The effects of honey processing on nanoparticles in *Astragali Radix* decoction: Self-assembly, bioavailability, and bioactivity, Food Res. Int. 218 (2025) 116877. https://doi.org/10.1016/j.foodres.2025.116877.

[22] O.Y. Mady, M.A. Osman, N.I. Sarhan, et al., Bioavailability enhancement of acyclovir by honey: Analytical and histological evidence, J. Drug Delivery Sci. Technol. 80 (2023) 104155. https://doi.org/10.1016/j.jddst.2023.104155.

[23] B. Xiao, Z. Sun, S.Y. Sun, et al., Effect of cortex mori on pharmacokinetic profiles of main isoflavonoids from pueraria lobata in rat plasma, J. Ethnopharmacol. 209 (2017) 140–146. https://doi.org/10.1016/j.jep.2017.07.035.

[24] M. Yousef, D.R. Brocks, R. Löbenberg, et al., Double peaking phenomena in pharmacokinetic disposition revisited, Clin. Pharmacokinet. 64 (2025). https://doi.org/10.1007/s40262-025-01559-4.

[25] A. Abeslami, H.E. Farissi, F. Cacciola, et al., Unveiling the mineral and sugar richness of Moroccan honeys: A study of botanical origins and quality indicators, Molecules 30 (2025) 150. https://doi.org/10.3390/molecules30010150.

[26] S. Valverde, A.M. Ares, J.S. Elmore, et al., Recent trends in the analysis of honey constituents, Food Chem. 387 (2022) 132920. https://doi.org/10.1016/j.foodchem.2022.132920.

[27] H. Wang, L. Li, X. Lin, et al., Composition, functional properties and safety of honey: a review, J. Sci. Food Agric. 103 (2023) 6767–6779. https://doi.org/10.1002/jsfa.12720.

[28] G.Z. Young, R. Blundell, A review on the phytochemical composition and health applications of honey, Heliyon 9 (2023) e12507. https://doi.org/10.1016/j.heliyon.2022.e12507.

[29] A. Mukhopadhyay, M. Rajput, A. Barui, et al., Dual cross-linked honey coupled 3D antimicrobial alginate hydrogels for cutaneous wound healing, Mater. Sci. Eng. C 116 (2020) 111218. https://doi.org/10.1016/j.msec.2020.111218.

[30] B. Yang, X. Wu, J. Zeng, et al., A Multi-Component Nano-Co-Delivery system utilizing Astragalus polysaccharides as carriers for improving biopharmaceutical properties of *Astragalus* flavonoids, Int. J. Nanomed. 18 (2023) 6705–6724. https://doi.org/10.2147/ijn.s434196.

[31] R. Maurya, A. Vikal, P. Patel, et al., "Enhancing oral drug absorption: Overcoming physiological and pharmaceutical barriers for improved bioavailability", AAPS PharmSciTech 25 (2024) 228. https://doi.org/10.1208/s12249-024-02940-5.

[32] I. Nyamba, C.B. Sombie, M. Yabre, et al., Pharmaceutical approaches for enhancing solubility and oral bioavailability of poorly soluble drugs, Eur. J. Pharm. Biopharm. 204 (2024) 114513. https://doi.org/10.1016/j.ejpb.2024.114513.

[33] P.B. Shekhawat, V.B. Pokharkar, Understanding peroral absorption: regulatory aspects and contemporary approaches to tackling solubility and permeability hurdles, Acta Pharm. Sin. B 7 (2017) 260–280. https://doi.org/10.1016/j.apsb.2016.09.005.

[34] H. Li, Y. Cao, L. Wang, et al., Pickering high internal phase emulsions stabilized by soy protein isolate/κ-carrageenan complex for enhanced stability, bioavailability, and absorption mechanisms of nobiletin, Carbohydr. Polym. 351 (2024) 123117. https://doi.org/10.1016/j.carbpol.2024.123117.

[35] R. Mukkavilli, C. Yang, R.S. Tanwar, et al., Absorption, metabolic stability, and pharmacokinetics of ginger phytochemicals, Molecules 22 (2017) 553. https://doi.org/10.3390/molecules22040553.

[36] U. Fagerholm, M. Johansson, H. Lennernäs, Comparison between permeability coefficients in rat and human jejunum, Pharm. Res. 13 (1996) 1336–1342. https://doi.org/10.1023/a:1016065715308.

[37] Y. Yao, W. Mi, G. Cao, et al., The absorption characteristics of nonvolatile components in a water extraction from Amomi fructus as determined by in situ single-pass intestinal perfusion and high-performance liquid chromatography, Front. Pharmacol. 11 (2020) 711. https://doi.org/10.3389/fphar.2020.00711.

[38] J. Zhang, D. Liu, Y. Huang, et al., Biopharmaceutics classification and intestinal absorption study of apigenin, Int. J. Pharm. 436 (2012) 311–317. https://doi.org/10.1016/j.ijpharm.2012.07.002.

[39] C.S. Chambers, J. Viktorová, K. Řehořová, et al., Defying multidrug resistance! Modulation of related transporters by flavonoids and flavonolignans, J. Agric. Food Chem. 68 (2019) 1763–1779. https://doi.org/10.1021/acs.jafc.9b00694.

[40] Y. Fang, W. Cao, F. Liang, et al., Structure affinity relationship and docking studies of flavonoids as substrates of multidrug-resistant associated protein 2 (MRP2) in MDCK/MRP2 cells, Food Chem. 291 (2019) 101–109. https://doi.org/10.1016/j.foodchem.2019.03.111.

[41] Y. Liu, Z. Zhang, X. Li, et al., Wogonin effects on the efflux transporters BCRP and MRP2, explain its effectiveness in ulcerative colitis: implications for metabolic and transport interactions, Pharmacol. Res. 212 (2024) 107570. https://doi.org/10.1016/j.phrs.2024.107570.

[42] P. Artursson, J. Karlsson, Correlation between oral drug absorption in humans and apparent drug permeability coefficients in human intestinal epithelial (Caco-2) cells, Biochem. Biophys. Res. Commun. 175 (1991) 880–885. https://doi.org/10.1016/0006-291x(91)91647-u.

[43] B. He, J. Bai, Z. Wu, Glucosamine enhances proliferation, barrier, and anti-oxidative functions in porcine trophectoderm cells, Food Funct. 13 (2022) 4551–4561. https://doi.org/10.1039/d1fo04086c.

[44] S. Luo, C. Terciolo, A.P.F. Bracarense, et al., *In vitro* and *in vivo* effects of a mycotoxin, deoxynivalenol, and a trace metal, cadmium, alone or in a mixture on the intestinal barrier, Environ. Int. 132 (2019) 105082. https://doi.org/10.1016/j.envint.2019.105082.

[45] M.S. Balda, K. Matter, Tight junctions, Curr. Biol. 33 (2023) R1135–R1140. https://doi.org/10.1016/j.cub.2023.09.027.

[46] W. Kuo, M.A. Odenwald, J.R. Turner, et al., Tight junction proteins occludin and ZO-1 as regulators of epithelial proliferation and survival, Ann. N. Y. Acad. Sci. 1514 (2022) 21–33. https://doi.org/10.1111/nyas.14798.

[47] K.S. Lynn, R.J. Peterson, M. Koval, Ruffles and spikes: Control of tight junction morphology and permeability by claudins, BBA - Biomembranes 1862 (2020) 183339. https://doi.org/10.1016/j.bbamem.2020.183339.

[48] E. Vasileva, D. Spadaro, F. Rouaud, et al., Cingulin binds to the ZU5 domain of scaffolding protein ZO-1 to promote its extended conformation, stabilization, and tight junction accumulation, J. Biol. Chem. 298 (2022) 101797. https://doi.org/10.1016/j.jbc.2022.101797.

[49] H.K. Campbell, J.L. Maiers, K.A. DeMali, Interplay between tight junctions & adherens junctions, Exp. Cell Res. 358 (2017) 39–44. https://doi.org/10.1016/j.yexcr.2017.03.061.

[50] S. Li, D. Zhang, Y. Li, et al., All-in-one multifunctional tri-block glycopolymers for targeted delivery of cisplatin and cancer chemotherapy, Colloids Surf. 252 (2025) 114639. https://doi.org/10.1016/j.colsurfb.2025.114639.

[51] H. Liu, J. Zou, X. Li, et al., Drug delivery for platinum therapeutics, J. Controlled Release 380 (2025) 503–523. https://doi.org/10.1016/j.jconrel.2025.02.006.